Ninth International Conference on CFD in the Minerals and Process Industries
CSIRO, Melbourne, Australia
10-12 December 2012

A FILTERED FRICTIONAL-KINETIC MODEL FOR GAS-SOLID FLUIDIZED AND MOVING BEDS

S. Schneiderbauer[1*], D. Schellander[1] and S. Pirker[1,2]

[1]Christian-Doppler Laboratory for Particulate Flow Modelling, Johannes Kepler University,
Altenbergerstr. 69, Linz, Austria
[2]Institute of Fluid Mechanics and Heat Transfer, Johannes Kepler University,
Altenbergerstr. 69, Linz, Austria
[*]Corresponding author, E-mail address: simon.schneiderbauer@jku.at

ABSTRACT

Due to increasing computer power the numerical simulation of fluidized and moving beds has become feasible. However, while kinetic theory based CFD (Computational Fluid Dynamics) has become a valuable design tool for modeling pilot plant scale gas-solid fluidized bed reactors, a fully resolved simulation of industrial scale reactor is still nearly unfeasible. It is, therefore, common to use sub-grid models to account for the effect of the small unresolved structures on large resolved scales when using coarse grids. Furthermore, state-of-the-art kinetic theory based CFD models for fluidized beds fail to predict the mass flow rates from hoppers and moving beds correctly, where frictional contacts between the particles dominate. We present a comprehensive frictional-kinetic model for fluidized and moving beds. A sub-grid drag correlation accounts for the drag reduction due to the formation of sub-grid particle clusters. In addition to a $\mu_i(I_s)$-rheology a dilation law is established in the frictional regime. Firstly, it is shown that in case of the coarse grid simulations the predicted bed expansion agrees excellently with fully resolved simulations. Secondly, the mass flow rate from a rectangular bin is in excellent agreement with measurements.

NOMENCLATURE

LATIN SYMBOLS

b, n_i	parameters for sub-grid drag ($i \in \{1,2,3\}$)
C_d	drag coefficient (see equ. (5))
$\mathbf{D}_q$	rate of deformation tensor for phase q
d_s, d_{cl}	particle diameter, cluster diameter
d, cl, c	superscripts denoting properties of the dilute, cluster and dense phase
e_s, e_w	coefficients of restitution for particle-particle and particle-wall collisions
$\boldsymbol{F}_d^{\mathrm{i}}$	sub-grid drag forces per unit volume
f^{d}, f^{c}	volume fractions of dilute and dense phase
g_0	radial distribution function
H_d	Heterogeneity index
I_s	inertial number (equ. (15))
$\boldsymbol{n}$	outwarding unit surface normal
p_s^{fr}, p_s^{kc}	solids pressures due to friction, due kinetic and collisional contributions
$\boldsymbol{q}$	flux of pseudo-thermal energy (equ. (10))
$\mathbf{S}_s$	solids stress tensor with frictional, $\mathbf{S}_s^{\mathrm{fr}}$, and a kinetic-collisional, $\mathbf{S}_s^{\mathrm{kc}}$, contribution
$\mathbf{T}_g$	shear stress tensor of the gas phase
Re_s	particle Reynolds number
$\boldsymbol{u}_g$, $\boldsymbol{u}_s$	local average velocity of gas and particle phase, respectively
$\boldsymbol{u}_s^{\mathrm{sl}}$	slip velocity

GREEK SYMBOLS

β_{WY}	interphase drag coefficient of Wen and Yu
β_e	effective drag coefficient
β_0	tangential restitution coefficient
ϵ_g, ϵ_s	volume fractions of interstitial gas and particles, respectively
$\epsilon_s^{\max}$	maximum packing ratio
γ_Θ	rate of dissipation of pseudo-thermal energy by inelastic collisions (equ. (10))
λ_s^{kc}	solids bulk viscosity from KTGF
μ_i, μ_w	coefficient of internal friction and of wall friction
μ_s	solids viscosity
ρ_g, ρ_s	densities of interstitial gas and solids, respectively
$\boldsymbol{\tau}_s$	solids wall shear stresses
Θ	granular temperature

INTRODUCTION

Fluidized beds and moving beds are widely used in process industries, for example, for biomass reactors, polymerization reactors, metallurgical processes and for the discharge of granular materials from silos. However, due to computational limitations a fully resolved simulation of industrial scale reactors is unfeasible (Parmentier et al., 2012). Andrews et al. (2005) suggested that a grid-independent solution can be obtained up to the grid size in the order of 10 particle diameters. In recent years, several approaches has been proposed to account for the effect of the small unresolved scales on the interphase momentum exchange when using two-fluid models with coarse realistic meshes. Igci and Sundaresan (2011) Parmentier et al. (2012) derive residual correlations from filtering fully resolved simulations. The EMMS approach (Lu et al., 2009; Hong et al., 2012) is based on the assumption that heterogenous structures form, which require additional modeling. The resulting underdetermined set of equations is solved by minimizing a cost function, referred to as stability condition. Finally, Wang et al. (2010) proposed a modification of homogenous drag models to account for heterogenous structures in bubbling fluidized beds, where the volume fraction of the bubbles is based on empirical correlations.

An adequate modeling of the unresolved part of the drag is essential to predict the correct bed expansion (Parmentier et al., 2012). In fact, the bed expansion appears to be nearly independent on the unresolved contribution of the particle stress. However, it has to be noted that although the magnitude of the drag force is much larger than the particle stresses, neglecting their unresolved contribution produces

quantitative changes in the predicted results (Igci and Sundaresan, 2011).

However, the general applicability of above mentioned modifications of homogenous drag correlations to bubbling fluidized beds is unverified. For example, the EMMS model was originally developed for risers. Igci and Sundaresan (2011) accounted for frictional stresses at solids volume fractions only above 0.59 when deriving the residual correlations for the effective drag. However, frictional stresses may become important even a significantly smaller solids volume fractions. Parmentier et al. (2012) introduced a shape parameter to match the results coarse grid simulations with corresponding fully resolved data.

In this paper, we present a filtered (effective) drag correlation for two-fluid models accounting for unresolved, i.e. sub-grid, structures in bubbling fluidized beds. In the next section the two-fluid model is presented, which the solids stress tensor is given by the addition of the collisional, kinetic and frictional stresses (Schneiderbauer et al., 2012a). After a detailed discussion of the effective drag, the model is tested for a bubbling fluidized bed of Geldard B particles. Finally, the discharge of particles from a rectangular bin is studied.

MODELLING GAS–PARTICLE FLOWS

In this paper, we use the two-fluid model approach for gas-particle flows presented in our previous study (Schneiderbauer et al., 2012a). The averaged continuity equation for phase q is written in equation (1). Note, equations (1) – (17) are summarized in table 1. In equation (1) $\boldsymbol{u}_q$ denotes the velocity, ϵ_q the volume fraction and ρ_q the density of phase q. In case of mono-disperse gas-particle flows q denotes either the gas phase g or the solid phase s. The averaged momentum equations for the gas-solid flow are given in equations (2) and (3). It is well established that the interphase momentum exchange coefficient, i.e. the drag coefficient β, of Wen and Yu (1966) well predicts rising bubbles and bed expansion (equation (5)), which is given in equation (5). Even during the discharge of Geldart B particles from a hopper the interphase momentum exchange plays an important role (Srivastava and Sundaresan, 2003). In equation (5) d_s denotes the diameter of the spherical grains, μ_g the molecular viscosity of the gas phase and Re_s the particle Reynolds number. However, (5) is only valid for homogeneously distributed particles, i.e. sub-grid effects such as clustering are negligible.

The stress-strain tensor for the gas phase, $\mathbf{T}_g$, in equation (7) is given by a simple Newtonian closure, where $\mathbf{D}_q$ denotes the rate-of-deformation tensor for phase q.

While in dense particulate flows the diffusive and convective transport of momentum is dominated by inter-particle collisions and inter-particle contacts (friction), in dilute particulate flows it is determined by the translational motion of the grains. If a huge number of particles is involved it will be practical to apply the kinetic theory of granular flows to close the solids stress tensor, $\mathbf{S}_s^{\mathrm{kc}}$, arising from kinetic and collisional contributions. This closure requires, analogous to the kinetic theory of gases, that the above set of equations be augmented by a balance of pseudo-thermal energy (PTE) of velocity fluctuations, E_{PTE} (Agrawal et al., 2001). The balance equation for E_{PTE} is given by equation (4), where $\Theta = 2/3 E_{PTE}$ denotes the granular temperature. Finally, the kinetic and collisional solids stress tensor, $\mathbf{S}_s^{\mathrm{kc}}$, is written in a compressible sense to account for the resistance of the granular particles to compression and expansion (equation (7)). Here, p_s^{kc} denotes the solids pressure (equation (13)), λ_s^{kc} the granular bulk viscosity (equation (13)) and μ_s^{kc} the kinetic-collisional granular viscosity (equation (8)).

In equation (4) the first term of the right hand side, $-\mathbf{S}_s^{\mathrm{kc}} : \boldsymbol{\nabla}\boldsymbol{u}_s$, determines the generation of pseudo-thermal engery. The second term, $-\boldsymbol{\nabla}\cdot\boldsymbol{q}$, represents the diffusion of pseudo-thermal energy, where the flux vector $\boldsymbol{q}$ is defined in equation (10). The transfer of the kinetic energy of random fluctuations in particle velocity from the solids phase to the gas phase is represented by the third, Γ_s, and forth term, J_v, on the right hand side of equation (4). The collisional dissipation, γ_Θ, represents the rate of dissipation of the pseudo-thermal energy, Θ, due to inelastic collisions between particles determined by the restitution coefficient e_s (equation (11)).

Equations (8) and (10) account for the role of the interstitial fluid by the terms μ^* and κ^*, respectively (Agrawal et al., 2001). Additionally, the presence of bounding walls is considered by $1/(1+l_s/\mathbb{L})$ constraining the mean free path of the particles, l_s, by a characteristic length scale, $\mathbb{L}$, of the actual physical system. At equilibrium the mean free path is given by $l_s = d_s/(6\sqrt{2}g_0\epsilon_s)$. The radial distribution function g_0 has to be introduced to the collisional integral in the Boltzmann equation to incorporate the maximum packing limit, $\epsilon_s^{\max}$, to the kinetic theory of granular flows. We follow Schneiderbauer et al. (2012a), who proposed equation (6) to comply $\|\mathbf{S}^{\mathrm{fr}}\| \gg \|\mathbf{S}^{\mathrm{kc}}\|$ in the frictional regime.

At high volume fractions ($\epsilon_s \gtrsim 0.4$, Forterre and Pouliquen, 2008) grains start to endure long, sliding and rubbing contacts, which gives rise to a totally different form of dissipation and stress, namely frictional. We follow our previous study (Schneiderbauer et al., 2012a) and write the particulate stress tensor, $\mathbf{S}_s$, as the sum of kinetic, collisional ($\mathbf{S}_s^{\mathrm{kc}}$) and frictional ($\mathbf{S}_s^{\mathrm{fr}}$) contributions, i.e. $\mathbf{S}_s = \mathbf{S}_s^{\mathrm{kc}} + \mathbf{S}_s^{\mathrm{fr}}$. In the frictional regime at high volume fractions the particle collisions are no longer instantaneous as assumed by kinetic theory. It is, therefore, concluded that an expression for the frictional part of the solids shear viscosity does not depend on the amount of pseudo-thermal energy. The frictional stress tensor is given by equation (7), where the frictional viscosity μ_s^{fr} is defined by equation (15). In our previous study (Schneiderbauer et al., 2012a) it was shown that a inertial number, I_s, dependent rheology $\mu_i(I_s)$ and a internal number dependent frictional pressure p_s^{fr} (equations (14) and (15)), which also includes shear rate dependent dilation, delivers the correct dependence of the discharge rate on the particle diameter in case of bin discharge. This is in contrast to state-of-the-art models as for example the Princeton model Srivastava and Sundaresan (2003). Typical values for the constants in equation (15) obtained for mono-dispersed glass beads are $I_0 = 0.279$, $\mu_i^{\mathrm{st}} = \tan(20.9^\circ)$ and $\mu_i^{\mathrm{c}} = \tan(32.76^\circ)$ (Forterre and Pouliquen, 2008). Equation (15) states that in the quasi-static regime ($I_s \lesssim 10^{-2}$) the effective friction coefficient, $\mu_i(I_s)$, is close to its minimum, μ_i^{st}. In the collisional regime ($I_s \gtrsim 10^{-1} - 10^{0}$) the friction coefficient saturates to μ_i^{c}. For mono-dispersed glass beads the constants in equation (14) take the values $\epsilon_s^{\max} \approx 0.6$ and $b \approx 0.2$ (Forterre and Pouliquen, 2008). Note that the frictional viscosity, μ_s^{fr}, diverges as $\mathrm{dev}\|\mathbf{D}_s\|$ tends to zero. This divergence ensures that a Drucker-Prager-like yield criterion exists. The frictional pressure diverges as well as the volume fraction tends to the volume fraction at maximum packing $\epsilon_s^{\max}$. Both divergences can be treated numerically by regularization techniques (Schneiderbauer et al., 2012a).

Following Schneiderbauer et al. (2012a) and Schneiderbauer et al. (2012b) the wall shear stresses, $\boldsymbol{\tau}_s^{\mathrm{kc}}$ and $\boldsymbol{\tau}_s^{\mathrm{fr}}$, and the flux of fluctuation energy at the bounding walls, $\boldsymbol{n}\cdot\boldsymbol{q}$, are given by equations (16)–(18). These boundary conditions incorporate sliding and non-sliding collisions. e_w and β_0 denote the normal and tangential particle-wall restitution coefficients. μ_w is the coefficient of wall friction and $\boldsymbol{n}$ the outwarding surface unit normal. In Schneiderbauer et al. (2012a) it was shown that these boundary conditions

Continuity equation, momentum equation and transport equation for pseudo-thermal energy:

$$\frac{\partial}{\partial t}\epsilon_q\rho_q + \boldsymbol{\nabla}\cdot(\epsilon_q\rho_q\boldsymbol{u}_q) = 0, \tag{1}$$

$$\frac{\partial}{\partial t}(\epsilon_g\rho_g\boldsymbol{u}_g) + \boldsymbol{\nabla}\cdot(\epsilon_g\rho_g\boldsymbol{u}_g\boldsymbol{u}_g) = -\epsilon_g\boldsymbol{\nabla}p + \boldsymbol{\nabla}\cdot\epsilon_g\mathbf{T}_g - \beta(\boldsymbol{u}_g-\boldsymbol{u}_s) + \epsilon_g\rho_g\boldsymbol{g}, \tag{2}$$

$$\frac{\partial}{\partial t}(\epsilon_s\rho_s\boldsymbol{u}_s) + \boldsymbol{\nabla}\cdot(\epsilon_s\rho_s\boldsymbol{u}_s\boldsymbol{u}_s) = -\epsilon_s\boldsymbol{\nabla}p - \boldsymbol{\nabla}\cdot\left(\mathbf{S}_s^{\mathrm{kc}}+\mathbf{S}_s^{\mathrm{fr}}\right) + \beta(\boldsymbol{u}_g-\boldsymbol{u}_s) + \epsilon_s\rho_s\boldsymbol{g}, \tag{3}$$

$$\frac{3}{2}\left(\frac{\partial}{\partial t}(\epsilon_s\rho_s\Theta) + \boldsymbol{\nabla}\cdot(\epsilon_s\rho_s\boldsymbol{u}_s\Theta)\right) = -\mathbf{S}_s^{\mathrm{kc}} : \boldsymbol{\nabla}\boldsymbol{u}_s - \boldsymbol{\nabla}\cdot\boldsymbol{q} + \Gamma_s - J_v - \gamma_\Theta. \tag{4}$$

Drag law:

$$\beta_{WY} = \frac{3}{4}C_d\frac{\epsilon_g\epsilon_s\rho_g\|\boldsymbol{u}_g-\boldsymbol{u}_s\|}{d_s}\epsilon_g^{-2.65}, \quad C_d = \begin{cases}\dfrac{24}{\mathrm{Re}_s}\left(1+0.15\mathrm{Re}_s^{0.687}\right) & \mathrm{Re}_s < 10^3 \\ 0.44 & \mathrm{Re}_s \geq 10^3\end{cases}, \quad \mathrm{Re}_s = \frac{\epsilon_g\rho_g\|\boldsymbol{u}_g-\boldsymbol{u}_s\|d_s}{\mu_g}. \tag{5}$$

Radial distribution function:

$$g_0 = \min\left(\frac{1}{1-\epsilon_s/\epsilon_s^{\max}}, \frac{1}{1-\epsilon_s}+\frac{3}{2}\frac{\epsilon_s}{(1-\epsilon_s)^2}+\frac{1}{2}\frac{\epsilon_s^2}{(1-\epsilon_s)^3}\right). \tag{6}$$

Gas-phase and solids phase stress tensors:

$$\mathbf{T}_g = 2\mu_g\mathbf{D}_g, \quad \mathbf{S}_s^{\mathrm{kc}} = \left(p_s^{\mathrm{kc}}-\lambda_s^{\mathrm{kc}}\mathrm{tr}(\mathbf{D}_s)\right)\mathbf{I} - 2\mu_s^{\mathrm{kc}}\mathrm{dev}\mathbf{D}_s, \quad \mathbf{S}_s^{\mathrm{fr}} = p_s^{\mathrm{fr}}\mathbf{I} - 2\mu_s^{\mathrm{fr}}\mathrm{dev}\mathbf{D}_s \tag{7}$$

$$\mathbf{D}_q = \frac{1}{2}\left(\boldsymbol{\nabla}\boldsymbol{u}_q + (\boldsymbol{\nabla}\boldsymbol{u}_q)^{\mathrm{T}}\right), \quad \mathrm{dev}\mathbf{D}_s = \mathbf{D}_s - \frac{1}{3}\mathrm{tr}(\mathbf{D}_s)\mathbf{I}.$$

Solids viscosity:

$$\mu_s^{\mathrm{kc}} = \left(\frac{2+\alpha}{3}\right)\left\{\frac{\mu^*}{g_0\eta_s(2-\eta_s)}\left(\frac{1}{1+\frac{l_s}{\mathbb{L}}}+\frac{8}{5}\epsilon_s\eta_s g_0\right)\left(1+\frac{8}{5}\eta_s(3\eta_s-2)\epsilon_s g_0\right)+\frac{3}{5}\eta_s\mu_b\right\}, \tag{8}$$

$$\mu^* = \frac{\mu}{1+\dfrac{2\beta\mu}{(\epsilon_s\rho_s)^2 g_0\Theta}}, \quad \mu = \frac{5\rho_s d_s\sqrt{\pi\Theta}}{96}, \quad \mu_b = \frac{256\mu\epsilon_s^2 g_0}{5\pi}, \quad \alpha = \frac{8}{5}, \quad \eta_s = \frac{1}{2}(1+e_s). \tag{9}$$

Pseudo-termal energy (PTE) flux vector $\boldsymbol{q}$, rate of dissipation of PTE γ_Θ, rate of dissipation of PTE by viscous damping J_v and rate of production of PTE by gas-particle slip Γ_s:

$$\boldsymbol{q} = -\frac{\kappa^*}{g_0}\left\{\left(\frac{1}{1+\frac{l_s}{\mathbb{L}}}+\frac{12}{5}\eta_s\epsilon_s g_0\right)\left(1+\frac{12}{5}\eta_s^2(4\eta_s-3)\epsilon_s g_0\right)+\frac{64}{25\pi}(41-33\eta_s)\eta_s^2\epsilon_s^2 g_0^2\right\}\boldsymbol{\nabla}\Theta, \tag{10}$$

$$\gamma_\Theta = \frac{48}{\sqrt{\pi}}\eta_s(1-\eta_s)\frac{\rho_s\epsilon_s^2}{d_s}g_0\Theta^{3/2}, \quad \kappa^* = \frac{\kappa}{1+\dfrac{6\beta\kappa}{5(\epsilon_s\rho_s)^2 g_0\Theta}}, \quad \kappa = \frac{75\rho_s d_s\sqrt{\pi\Theta}}{48\eta_s(41-33\eta_s)}, \tag{11}$$

$$\Gamma_s = \frac{81\epsilon_s\mu_g^2\|\boldsymbol{u}_g-\boldsymbol{u}_s\|}{g_0 d_s^3\rho_s\sqrt{\pi\Theta}}, \quad J_v = 3\beta\Theta \tag{12}$$

Solids pressure and bulk viscosity:

$$p_s^{\mathrm{kc}} = \epsilon_s\rho_s\left(\frac{1}{1+\frac{l_s}{\mathbb{L}}}+4\eta_s\epsilon_s g_0\right)\Theta, \quad \lambda_s^{\mathrm{kc}} = \frac{8}{3}\eta_s\epsilon_s^2\rho_s d_s g_0\sqrt{\frac{\Theta}{\pi}}. \tag{13}$$

Frictional pressure and viscosity:

$$p_s^{\mathrm{fr}} = 4\rho_s\left(\frac{bd_s\|\mathrm{dev}\mathbf{D}_s\|}{\epsilon_s^{\max}-\epsilon_s}\right)^2, \tag{14}$$

$$\mu_s^{\mathrm{fr}}(I_s, p_s^{\mathrm{fr}}, \mathrm{dev}\mathbf{D}_s) = \frac{\mu_i(I_s)p_s^{\mathrm{fr}}}{2\|\mathrm{dev}\mathbf{D}_s\|}, \quad \mu_i(I_s) = \mu_i^{\mathrm{st}} + \frac{\mu_i^{\mathrm{c}}-\mu_i^{\mathrm{st}}}{I_0/I_s+1}, \quad I_s = \frac{2\|\mathrm{dev}\mathbf{D}_s\|d_s}{\sqrt{p_s^{\mathrm{fr}}/\rho_s}}. \tag{15}$$

Boundary conditions for particulate phase in the collisional regime:

$$\boldsymbol{\tau}_s^{\mathrm{kc}} = -\eta_w\mu_w\epsilon_s\rho_s g_0\Theta\,\mathrm{erf}(\bar{u}_s)\frac{\boldsymbol{u}_s^{\mathrm{sl}}}{\|\boldsymbol{u}_s^{\mathrm{sl}}\|}, \quad \mu_0 = \frac{7}{2}\frac{1+e_w}{1+\beta_0}\mu_w, \quad \eta_w = \frac{1}{2}(1+e_w) \quad \bar{u}_s = \frac{\|\boldsymbol{u}_s^{\mathrm{sl}}\|}{\sqrt{2\Theta}\mu_0}, \tag{16}$$

$$\boldsymbol{n}\cdot\boldsymbol{q} = \boldsymbol{\tau}_s^{\mathrm{kc}}\cdot\boldsymbol{u}_s^{\mathrm{sl}} - \frac{\epsilon_s\rho_s g_0\eta_w\sqrt{\Theta}}{\sqrt{2}\mu_0^2\sqrt{\pi}}\exp(-\bar{u}_s^2)\left\{\mu_w\left[2\mu_w\|\boldsymbol{u}_s^{\mathrm{sl}}\|^2(2\eta_w-\mu_0)+\Theta\Big(14\mu_w\eta_w-4\mu_0(1+\mu_w)-6\mu_w\mu_0^2\eta_w\Big)\right]\right. \tag{17}$$

$$\left.+\,\mu_0^2\sqrt{\Theta}\exp(\bar{u}_s^2)\left[\sqrt{\Theta}(4(\eta_w-1)+6\mu_w^2\eta_w)-\sqrt{2\pi}\mu_w\|\boldsymbol{u}_s^{\mathrm{sl}}\|\,\mathrm{erf}(\bar{u}_s)\right]\right\}.$$

Boundary conditions for particulate phase in the frictional regime:

$$\boldsymbol{\tau}_s^{\mathrm{fr}} = -\frac{\boldsymbol{u}_s^{\mathrm{sl}}}{\|\boldsymbol{u}_s^{\mathrm{sl}}\|}\begin{cases}\tau_s^{\mathrm{fr,ns}} & \tau_s^{\mathrm{fr,ns}} < \tau_s^{\mathrm{fr,sl}} \\ \tau_s^{\mathrm{fr,sl}} & \text{else}\end{cases} \quad \text{with} \quad \begin{array}{l}\tau_s^{\mathrm{fr,sl}} = \mu_w\left\|\boldsymbol{n}\cdot\mathbf{S}_s^{\mathrm{fr}}\cdot\boldsymbol{n}\right\| \\ \tau_s^{\mathrm{fr,ns}} = \left\|\mathbf{S}_s^{\mathrm{fr}}\cdot\boldsymbol{n}-\left(\boldsymbol{n}\cdot\mathbf{S}_s^{\mathrm{fr}}\cdot\boldsymbol{n}\right)\cdot\boldsymbol{n}\right\|\end{array} \tag{18}$$

Table 1: Model equations for gas-particle flows (Schneiderbauer et al., 2012a).

apply well to multiple-spout pseudo-2D fluidized beds and moving beds.

SUB-GRID DRAG LAW

It is common to solve the model equations given in table (1) by discretizing these equations in space by using a finite volume grid and in time by using finite differences. The spatial discretization of the transport equations (1)–(4) yields corresponding equations for the resolved parts of the transport variables. Such a discretization can be regarded as a filtering operation of a continuous space-time variable $g(\boldsymbol{x}, t)$ reading as (Parmentier et al., 2012)

$$\bar{g}(\boldsymbol{x}, t) = \iiint G(\boldsymbol{x} - \boldsymbol{y}) g(\boldsymbol{y}, t)\, \mathrm{d}\boldsymbol{y}, \tag{19}$$

where $G(\boldsymbol{x}-\boldsymbol{y})$ denotes a weight function given by the discretization that satisfies $\iiint G(\boldsymbol{x} - \boldsymbol{y})\, \mathrm{d}\boldsymbol{y} = 1$. $\bar{g}(\boldsymbol{x}, t)$ is the filtered part of $g(\boldsymbol{y}, t)$ and is, therefore, the discretized or resolved part. By applying equation (20) to the momentum equations (2) and (3) additional terms representing the unresolved contributions arise. Parmentier et al. (2012) showed that the unresolved part of the drag has to be modeled adequately to predict the correct bed expansion. Following their study the filtered drag force can be modeled by a multiplicative approach

$$\bar{\beta} = \bar{\beta}_{WY} H_d, \tag{20}$$

where H_d is a function accounting for the unresolved structures. $\bar{\beta}_{WY}$ denotes the drag correlation of Wen and Yu (1966) computed from filtered variables. According to the EMMS group H_d can be considered as heterogeneity index. It has to be mentioned that for sufficiently small grid spacings, that is $\Delta \lesssim 10 d_s$, $H_d \approx 1$ (Andrews et al., 2005). Note that we skip the overbars indicating filtered variables in the preceding discussion for better readability.

To obtain an expression for H_d we follow the idea of the EMMS model assuming the heterogeneity inside fluidized beds is caused by the formation of local clusters. Inside (dense phase) and outside (dilute phase) a cluster the particles are considered as homogeneously distributed (figure 1). The corresponding pressure balance between clusters and

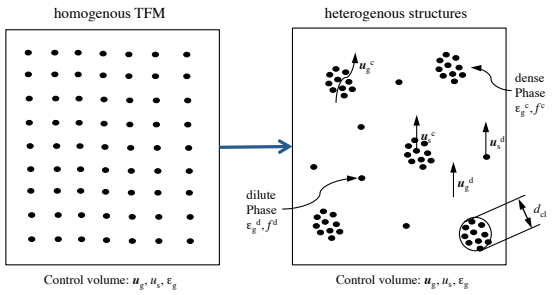

Figure 1: . The schematic diagram of the sub-grid heterogeneity (Hong et al., 2012).

dilute phase reads (Wang et al., 2008; Hong et al., 2012)

$$\boldsymbol{F}_d^{\mathrm{d}} + \frac{1}{f^{\mathrm{d}}} \boldsymbol{F}_d^{\mathrm{cl}} = \boldsymbol{F}_d^{\mathrm{c}}. \tag{21}$$

with

$$\begin{aligned}
\boldsymbol{F}_d^{\mathrm{d}} &= \frac{3}{4} C_d^{\mathrm{d}} \frac{\rho_g \epsilon_g^{\mathrm{d}} \epsilon_s^{\mathrm{d}}}{d_s} \|\boldsymbol{u}_g^{\mathrm{d}} - \boldsymbol{u}_s^{\mathrm{d}}\| (\boldsymbol{u}_g^{\mathrm{d}} - \boldsymbol{u}_s^{\mathrm{d}}), \\
\boldsymbol{F}_d^{\mathrm{cl}} &= \frac{3}{4} C_d^{\mathrm{cl}} \frac{\rho_g \epsilon_g \epsilon_s}{d_{cl}} \|\boldsymbol{u}_g^{\mathrm{d}} - \boldsymbol{u}_s^{\mathrm{c}}\| (\boldsymbol{u}_g^{\mathrm{d}} - \boldsymbol{u}_s^{\mathrm{c}}), \\
\boldsymbol{F}_d^{\mathrm{c}} &= \frac{3}{4} C_d^{\mathrm{c}} \frac{\rho_g \epsilon_g^{\mathrm{c}} \epsilon_s^{\mathrm{c}}}{d_s} \|\boldsymbol{u}_g^{\mathrm{c}} - \boldsymbol{u}_s^{\mathrm{c}}\| (\boldsymbol{u}_g^{\mathrm{c}} - \boldsymbol{u}_s^{\mathrm{c}}).
\end{aligned} \tag{22}$$

$\boldsymbol{F}_d^{\mathrm{d}}$ and $\boldsymbol{F}_d^{\mathrm{cl}}$ denote the drag forces per unit volume of the dilute and the dense phase, respectively. The drag force $\boldsymbol{F}_d^{\mathrm{cl}}$ arises from the interaction between the surrounding dilute-phase gas and the dense-phase particles. The superscripts d, c and cl refer to the dilute phase, the dense phase and the particle clusters of diameter d_{cl} (see also figure 1). Since the particles and clusters are homogeneously distributed the drag coefficients for particles in the dilute phase, C_d^{d}, for particles in the dense phase (cluster), C_d^{c}, and for the clusters, C_d^{cl}, can be closed by, for example, using Wen and Yu (1966)

$$C_d^{\mathrm{i}} = \frac{24}{\mathrm{Re}_s^{\mathrm{i}}} \left(1 + 0.15 (\mathrm{Re}_s^{\mathrm{i}})^{0.687}\right) (\epsilon_g^{\mathrm{i}})^{-2.65}, \tag{23}$$

$$C_d^{\mathrm{cl}} = \frac{24}{\mathrm{Re}_s^{\mathrm{cl}}} \left(1 + 0.15 (\mathrm{Re}_s^{\mathrm{cl}})^{0.687}\right) \epsilon_g^{-2.65} \tag{24}$$

with the Reynolds numbers

$$\mathrm{Re}_s^{\mathrm{i}} = \frac{\epsilon_g^{\mathrm{i}} \rho_g \|\boldsymbol{u}_g^{\mathrm{i}} - \boldsymbol{u}_s^{\mathrm{i}}\| d_s}{\mu_g}, \; \mathrm{Re}_s^{\mathrm{cl}} = \frac{\epsilon_g \rho_g \|\boldsymbol{u}_g^{\mathrm{d}} - \boldsymbol{u}_s^{\mathrm{c}}\| d_{cl}}{\mu_g},$$

where $\mathrm{i} \in \{\mathrm{d}, \mathrm{c}\}$. f^{c} denotes the volume fraction of the dense phase, that is the volume fraction of the clusters, which is connected to the volume fraction of the dilute phase as follows $f^{\mathrm{d}} = 1 - f^{\mathrm{c}}$. The effective drag coefficient, β_e, accounting for the heterogeneity can be derived from equation (22) yielding

$$\beta_e = \frac{1}{\|\boldsymbol{u}_g - \boldsymbol{u}_s\|} \left\| f^{\mathrm{d}} \boldsymbol{F}_d^{\mathrm{d}} + \boldsymbol{F}_d^{\mathrm{cl}} + f^{\mathrm{c}} \boldsymbol{F}_d^{\mathrm{c}} \right\|. \tag{25}$$

Note that equation (25) is compatible with equations (2) and (3). According to equation (25) H_d equals β_e / β_{WY} in our study and thus, the filtered drag reads $\beta = \beta_e$. Additionally, $\boldsymbol{u}_g^{\mathrm{i}}$ and $\boldsymbol{u}_s^{\mathrm{i}}$ ($\mathrm{i} \in \{\mathrm{d}, \mathrm{c}\}$) satisfy the mass conservation for the fluid (Wang et al., 2008; Hong et al., 2012)

$$\epsilon_g \boldsymbol{u}_g = \epsilon_g^{\mathrm{d}} \boldsymbol{u}_g^{\mathrm{d}} f^{\mathrm{d}} + \epsilon_g^{\mathrm{c}} \boldsymbol{u}_g^{\mathrm{c}} f^{\mathrm{c}} \tag{26}$$

and for the particle phase

$$\epsilon_s \boldsymbol{u}_s = \epsilon_s^{\mathrm{d}} \boldsymbol{u}_s^{\mathrm{d}} f^{\mathrm{d}} + \epsilon_s^{\mathrm{c}} \boldsymbol{u}_s^{\mathrm{c}} f^{\mathrm{c}}. \tag{27}$$

Furthermore, the mean voidage ϵ_g is given by

$$\epsilon_g = \epsilon_g^{\mathrm{d}} f^{\mathrm{d}} + \epsilon_g^{\mathrm{c}} f^{\mathrm{c}}. \tag{28}$$

However, obviously the set of equations (21), (26), (27) and (28) (10 equations) is not closed and, thus, β_e can not be computed from equation (25). In detail, we have 18 unknowns, these are $\boldsymbol{u}_g^{\mathrm{i}}$, $\boldsymbol{u}_s^{\mathrm{i}}$, ϵ_g^{i}, ϵ_s^{i}, f^{c} and d_{cl}, which can be reduced to 16 by using $\epsilon_s^{\mathrm{i}} = 1 - \epsilon_g^{\mathrm{i}}$.

For Geldart B and D particles it is reasonable to assume that $\mathcal{O}(\epsilon_s^{\mathrm{d}}) \ll \mathcal{O}(\epsilon_s^{\mathrm{c}})$ (Wang et al., 2010), which implies $\epsilon_g^{\mathrm{d}} \approx 1$. In this case, $\epsilon_s^{\mathrm{d}} \boldsymbol{u}_s^{\mathrm{d}} f^{\mathrm{d}} \ll \epsilon_s^{\mathrm{c}} \boldsymbol{u}_s^{\mathrm{c}} f^{\mathrm{c}}$ and this, in turn, implies $\epsilon_s^{\mathrm{c}} \boldsymbol{u}_s^{\mathrm{c}} f^{\mathrm{c}} \approx \epsilon_s \boldsymbol{u}_s$. By using $\epsilon_s^{\mathrm{c}} f^{\mathrm{c}} \approx \epsilon_s$ equations (26), (27) and (28) reduce to

$$\epsilon_g \boldsymbol{u}_g = \boldsymbol{u}_g^{\mathrm{d}} f^{\mathrm{d}} + \epsilon_g^{\mathrm{c}} \boldsymbol{u}_g^{\mathrm{c}} f^{\mathrm{c}}, \tag{29}$$

$$\boldsymbol{u}_s = \boldsymbol{u}_s^{\mathrm{c}}, \tag{30}$$

$$\epsilon_g = f^{\mathrm{d}} + \epsilon_g^{\mathrm{c}} f^{\mathrm{c}}. \tag{31}$$

In this limit $\boldsymbol{F}_d^{\mathrm{d}}$ is negligible compared to $\boldsymbol{F}_d^{\mathrm{cl}}$ and $\boldsymbol{F}_d^{\mathrm{c}}$ and, hence, equation (21) yields

$$\boldsymbol{F}_d^{\mathrm{cl}} \approx f^{\mathrm{d}} \boldsymbol{F}_d^{\mathrm{c}}. \tag{32}$$

If the voidage within clusters, ϵ_g^{c}, is known, the fraction of clusters can be computed from equation (31) as follows

$$f^{\mathrm{c}} = \frac{1-\epsilon_g}{1-\epsilon_g^{\mathrm{c}}} = \frac{\epsilon_s}{\epsilon_s^{\mathrm{c}}}. \tag{33}$$

Wang et al. (2008) proposed that

$$\epsilon_g^{\mathrm{c}} = \epsilon_s - n\sigma_\epsilon, \tag{34}$$

where σ_ϵ denotes the standard deviation of the fluctuations of the solids volume fraction. Based on a doubly stochastic Poisson process, i.e. the number of particles in a cluster follows a negative exponential distribution (Zou et al., 1994) and these randomly distributed particles inside a cluster follow a Poisson distribution, they calculated σ_ϵ as

$$\sigma_\epsilon = \epsilon_s \sqrt{S(\epsilon_s)}, \tag{35}$$

where $S(\epsilon_s)$ is the static structure factor in the small wave vector limit written as

$$S(\epsilon_s) = \frac{(1-\epsilon_s)^4}{1+4\epsilon_s+4\epsilon_s^2-4\epsilon_s^3+\epsilon_s^4}. \tag{36}$$

Furthermore, the probability density function of the normalized cluster diameter, $\xi = d_{cl}/d_s$ can be expressed as follows (Zou et al., 1994)

$$p(\xi) = A \exp\left(-\frac{(\xi-1)^b}{\delta}\right) \tag{37}$$

with $\delta = \epsilon_s^{n_1}(\epsilon_s^{\mathrm{mf}} - \epsilon_s)^{-n_2}\epsilon_g^{-n_3}$ and A is determined by $\int_1^\infty p(\xi)\,\mathrm{d}\xi = 1$. ϵ_s^{mf} denotes the solids volume fraction at minimum fluidization conditions. By experimental correlation the following parameters were obtained: $b = 0.72$, $n_1 = 0.25$, $n_2 = 2.41$ and $n_3 = 1.5$. The average cluster diameter as a function of the solids volume fraction is, therefore, given by (Zou et al., 1994)

$$\langle\xi\rangle_\infty = \int_1^\infty \xi p(\xi)\,\mathrm{d}\xi \approx 1.8543\delta^{1.3889} + 1. \tag{38}$$

It is observed that the mean cluster diameter is a monotonically increasing function with the mean solids volume fraction and diverges at ϵ_s^{mf}. Physically, this behavior is reasonable since above ϵ_s^{mf}, where no fluidization occurs, the homogenous distribution of the particles is recovered. However, clusters greater than the grid spacing Δ are resolved by the grid and, therefore, require no additional modeling. In this case, according to the assumption of homogeneously distributed particles inside a cluster, homogenous conditions in a numerical cell establish and β_{WY} (equation (5)) would be applicable directly. Therefore, we propose to use the expectation value of the unresolved clusters for d_{cl}, that is

$$d_{cl} = d_s\langle\xi\rangle_\Delta \quad \text{with} \quad \langle\xi\rangle_\Delta = \int_1^{\Delta/d_s} \xi p(\xi)\,\mathrm{d}\xi. \tag{39}$$

The antiderivative in equation (39) can be evaluated by the substitution $\zeta = \xi - 1$, which yields

$$d_{cl} = d_s \int_0^{\Delta/d_s - 1} (\zeta+1)p(\zeta)\,\mathrm{d}\zeta. \tag{40}$$

Integration gives

$$d_{cl} = d_s \frac{\Gamma(\bar{b}) - \Gamma(\bar{b},\bar{\Delta}) + \delta^{1/b}\big(\Gamma(2\bar{b}) - \Gamma(2\bar{b},\bar{\Delta})\big)}{b\Gamma(1+\bar{b})}. \tag{41}$$

with

$$\bar{b} = b^{-1} \quad \text{and} \quad \bar{\Delta} = \left(\frac{\Delta}{d_s} - 1\right)^b \delta^{-1}.$$

$\Gamma(a,z)$ denotes the incomplete Gamma function given by

$$\Gamma(a,z) = \int_z^\infty t^{a-1}e^{-t}\,\mathrm{d}t.$$

Note that $\Gamma(a) = \Gamma(a,0)$. As Δ approaches ∞, d_{cl} tends to result of equation (38), that is

$$\lim_{\Delta\to\infty} d_{cl} = d_s\langle\xi\rangle_\infty.$$

In figure 2 the expectation value of the dimensionless cluster diameter $\langle\xi\rangle_\Delta = d_{cl}/d_s$ is plotted as a function of the mean voidage ϵ_g. The figure shows that for grid spacings of $\mathcal{O}(\Delta) < \mathcal{O}(10d_s)$ the unresolved clusters only affect regions of high voidage, i.e. $\epsilon_g > 0.85$. Thus, in case of fluidized beds, where regions of low voidage are predominant, a homogenous drag law can be applied for grid spacings $\Delta < 10d_s$ (Andrews et al., 2005). In contrast, for grid spacings of $\mathcal{O}(\Delta) > \mathcal{O}(100d_s)$ clusters containing a huge number of particles are present for nearly the whole range of ϵ_g indicating pronounced heterogenous sub-grid structures, which require additional modeling in the sense of equations (29)–(32).

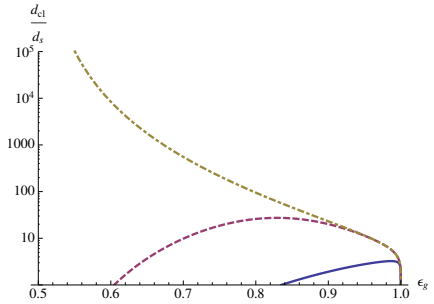

Figure 2: The dimensionless average cluster diameter $\langle\xi\rangle_\Delta = d_{cl}/d_s$ as a function of the mean voidage ϵ_g ($\epsilon_s^{\mathrm{mf}} = 0.5$) for different grid spacings Δ: — $10d_s$; – – $100d_s$; – · – ∞.

To sum up, we have closed the system of equations (29)–(32) by assumptions about the void fraction inside a cluster (equation (34)) and the mean unresolved cluster diameter (equation (41)). However, the fluid velocity in the dilute region, $\boldsymbol{u}_g^{\mathrm{d}}$, and the fluid velocity inside a cluster, $\boldsymbol{u}_g^{\mathrm{d}}$ remain unknown. These can be obtained from the following nonlinear system of equations

$$\boldsymbol{G}(\boldsymbol{u}_g^{\mathrm{d}}, \boldsymbol{u}_g^{\mathrm{c}}) = \begin{pmatrix} \epsilon_g\boldsymbol{u}_g - \boldsymbol{u}_g^{\mathrm{d}}f^{\mathrm{d}} - \epsilon_g^{\mathrm{c}}\boldsymbol{u}_g^{\mathrm{c}}f^{\mathrm{c}} \\ \boldsymbol{F}_d^{\mathrm{cl}} - f^{\mathrm{d}}\boldsymbol{F}_d^{\mathrm{c}} \end{pmatrix} = 0. \tag{42}$$

with $\boldsymbol{u}_s = \boldsymbol{u}_s^{\mathrm{c}}$ and $f^{\mathrm{d}} + f^{\mathrm{c}} = 1$. Equation (42) can be solved iteratively by applying Newton's method or Broydon's method.

Finally, the effective drag coefficient including sub-grid structures may read as

$$\beta_e = \frac{1}{\|\boldsymbol{u}_g - \boldsymbol{u}_s\|}\left\|\boldsymbol{F}_d^{\mathrm{cl}} + f^{\mathrm{c}}\boldsymbol{F}_d^{\mathrm{c}}\right\|, \tag{43}$$

where $\boldsymbol{F}_d^{\mathrm{cl}}$ and $\boldsymbol{F}_d^{\mathrm{d}}$ can be computed from the solution of equation (42).

In figure 3 the heterogeneity index $H_d = \beta_e/\beta_{WY}$ for equation (43) is plotted. Firstly, the figure shows is that

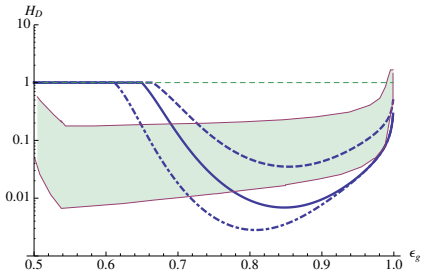

Figure 3: Heterogeneity index $H_d = \beta_e/\beta_{WY}$ for $\rho_s = 930\,\mathrm{kg\,s^{-1}}$ and $d_s = 54\,\mu\mathrm{m}$ as a function of the mean voidage ϵ_g for different grid spacings Δ and slip velocities $u_s^{\mathrm{sl}} = \|\boldsymbol{u}_g - \boldsymbol{u}_s\|$: — $\Delta = 100d_s$, $u_s^{\mathrm{sl}} = 0.1\,\mathrm{m\,s^{-1}}$; – – $\Delta = 100d_s$, $u_s^{\mathrm{sl}} = 15\,\mathrm{m\,s^{-1}}$; – · – $\Delta = 200d_s$, $u_s^{\mathrm{sl}} = 0.1\,\mathrm{m\,s^{-1}}$. The shaded area between the thin lines correspond to the EMMS/matrix model (extracted from Lu et al., 2009) covering a slip velocity range of $0.001 < u_s^{\mathrm{sl}} < 15.2\,\mathrm{m\,s^{-1}}$.

$H_d \ll 1$, i.e. compared to the homogeneous correlation β_{WY} the effective drag β_e is significantly reduced, at voidages ϵ_g with large unresolved clusters. Secondly, H_d increases for increasing slip velocity u_s^{sl}, which is in accordance with the predictions of the EMMS model. Finally, H_d decreases for increasing grid spacing Δ, since the expectation value of the diameter of the unresolved clusters increases as well. This is in contrast to the EMMS model, which does not distinguish between resolved and unresolved clusters. This, in turn, implies that EMMS predicts a significantly lower heterogeneity index in the dense regime (low voidage), where the clusters are resolved by the grid, than the presented model. However, around the solids volume fraction at minimum fluidization conditions the prevailing frictional stresses may also homogenize the granular assembly and, therefore, H_d tends to unity around ϵ_s^{mf} as predicted by the presented model.

BUBBLING FLUIDIZED BED

To validate the presented sub-grid drag correlation we studied a gas-solid bubbling fluidized bed of Geldart B particles with a diameter of $d_s = 150\,\mu\mathrm{m}$ and a density of $\rho_s = 2500\,\mathrm{kg\,m^{-3}}$. The gas density was $\rho_s = 2500\,\mathrm{kg\,m^{-3}}$ and the inflow gas velocity was set to $u_g^{\mathrm{in}} = 0.3\,\mathrm{m^{-1}}$. The remaining model parameters were set to $\epsilon_s^{\mathrm{mf}} = 0.5$, $\epsilon_s^{\mathrm{max}} = 0.6$, $\mu_w = 0.5$, $e_s = 0.9$, $e_w = 0.9$ and $\beta_0 = 0.4$ (Schneiderbauer et al., 2012a). The dimensions of the fluidized bed are $150\times40\times2500$ mm and the initial bed height was chosen 0.5 m.

We obtained a time-dependent solution using a grid spacing $\Delta = 8d_s$, which is assumed to be sufficiently fine to resolve all heterogeneous structures (Andrews et al., 2005), referred to as reference solution. Thus, we used the homogenous drag correlation in equation (5) since $\beta_e \equiv \beta_{WY}$ for $\Delta \leq 10d_s$ in case of fluidized beds. To study the impact of disregarding sub-grid structures on the behavior of the fluidized bed, that is for example the bed expansion, we repeated this simulation using a grid spacing of $\Delta = 100d_s$ (coarse grid). In figure 4 a comparison of the time-averaged axial profile of the filtered solids volume fraction ϵ_s is shown. It is observed that neglecting sub-grid inhomogeneities leads to a significant over-prediction of the bed expansion using the coarse grids. In fact, the bed expansion is overestimated by about 80% compared to the fully resolved reference simulation. Furthermore, figure 5 shows that the coarse grid simulation generally underestimates the standard deviation of the filtered solids volume fraction. This indicates that the bubbling of the fluidized bed is less pronounced using the coarse grid. In other words, the particles are predicted to be less heterogeneously distributed and no distinct bubbles form, which is also confirmed by comparing snapshots of the spatial distribution of the solids volume fraction (figure 6).

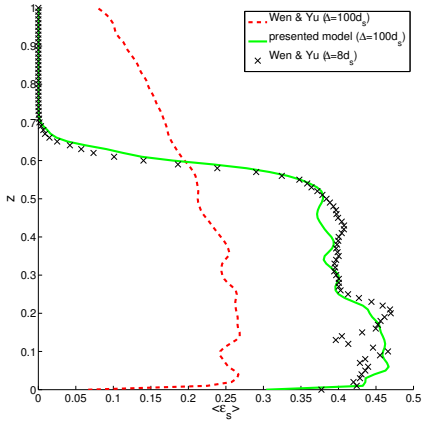

Figure 4: Axial profile of the time averaged filtered solids volume fraction, ϵ_s. The averaging time is 10 s (z in m).

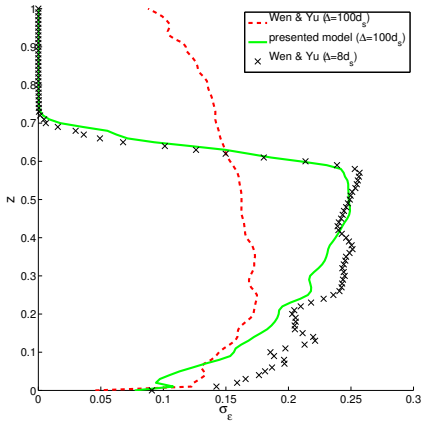

Figure 5: Axial profile of the standard deviation of the filtered solids volume fraction, σ_ϵ. The averaging time is 10 s (z in m).

Finally, we studied the behavior of the fluidized bed using the presented effective drag correlation (equation (43)) using the coarse grid ($\Delta = 100d_s$). Figure 4 clearly demonstrates that the bed expansion is predicted correctly using the coarse grid if sub-grid structures are considered. In addition, the presented drag model predicts the axial time-averaged profile of the solids volume fraction appropriately, which is characterized by higher particle concentrations in the gas-inflow area, i.e. $\langle\epsilon_s\rangle \approx 0.45$ for $z < 0.3$ m, and lower particle concentrations at lower hydrostatic pressure, i.e. $\langle\epsilon_s\rangle \approx 0.4$ for $z > 0.3$ m. Even though the standard deviation of the solids volume fraction differs from the fully resolved simulation up to 50% in the gas-inflow area, the amount bubbling and the formation of distinct bubbles is recovered by the coarse grid simulation using the presented effective drag (figure 6). Especially for $z > 0.2$ m the figure shows a good correlation between both simulations.

DISCHARGE FROM A BIN

In figure 7 the computed discharge rates from a rectangular bin using the presented frictional closure closure for $\mathbf{S}_s^{\mathrm{fr}}$

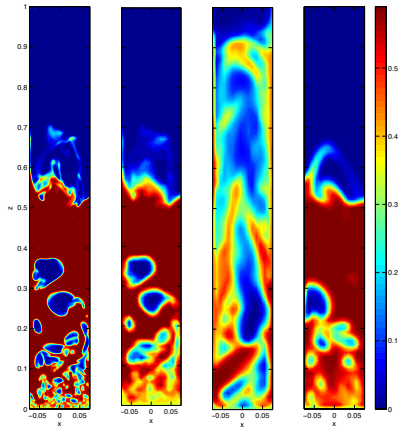

(a) (b) (c) (d)

Figure 6: Snapshot of the filtered solids volume fraction, ϵ_s, at $t = 10\,\mathrm{s}$ (z in m). a) fully resolved, b) fully resolved displayed on the coarse grid, c) coarse grid using β_{WY} (equation (5)) and d) coarse grid using β_e (equation (43)).

are compared to the experimental results. Note numerical settings, dimensions of the bin and experimental data can be found in Schneiderbauer et al. (2012a). The discharge rates obtained by the presented rheological model agree very accurately with the experiment for each particle diameter. Even though the discharge rate of the $4\,\mathrm{mm}$ particles is predicted correctly. In this case, the particle diameter is comparable with the width w of the exit orficie, that is $w = 10\,\mathrm{mm}$.

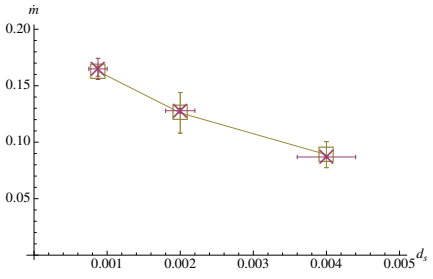

Figure 7: Discharge rates $\dot{m}$ in $\mathrm{kg\,s^{-1}}$ from a rectangular bin as a function of the particle diameter d_s in m; $\times$: discharge measurements; $\square$: $\mathbf{S}_s^{\mathrm{fr}}$ closed by $\mu_i(I_s)$-rheology (results from Schneiderbauer et al., 2012a). The horizontal error bars correspond to the standard deviations of the glass beads, the vertical error bars correspond to the simulated discharge rates.

CONCLUSIONS AND OUTLOOK

In this paper, we have introduced a new closure for the heterogeneity index H_d, that is the correction of a homogenous drag correlation to account for sub-grid structures. Its derivation is based on the assumption about the formation of clusters. In contrast to EMMS, which is also fundamentally based on the cluster concept, we distinguish between resolved and unresolved clusters. Furthermore, we assumed that the solids volume within the dilute phase is negligibly small leading to a closed set of equation for the heterogeneity index. Finally, we investigated the discharge from a rectangular bin.

The results show applying a homogenous drag law fails to predict the bed expansion using a finite volume mesh with a grid spacing of 100 particle diameters. It is further observed that in this case the simulation delivers a completely different behavior of the fluidized bed (for example bubble size and form) compared to the fully resolved case. In contrast, applying the presented filtered drag correlation yields excellent agreement of predicted bed expansion and bed behavior with the fully resolved simulation.

The frictional closure was additionally validated by measurements of the discharge rates from a rectangular bin. It was shown that the model predicts the discharge rates very accurately even for particles with a diameter in the order of the dimensions of the exit orifice.

Future work will concentrate on testing the presented drag correction in different flow regimes as, for example, for varying inflow gas velocities. Furthermore, the applicability of the model to different grid size to particle diameter ratios Δ/d_s and to Geldart A particles should be studied.

ACKNOWLEDGEMENTS

This work was funded by the Christian-Doppler Research Association, the Austrian Federal Ministry of Economy, Family and Youth, the Austrian National Foundation for Research, Technology and Development.

REFERENCES

K. Agrawal, P. N. Loezos, M. Syamlal, and S. Sundaresan. The role of meso-scale structures in rapid gas-solid flows. *Journal of Fluid Mechanics*, 445:151–185, October 2001.

A. T. Andrews, P. N. Loezos, and S. Sundaresan. Coarse-Grid Simulation of Gas-Particle Flows in Vertical Risers. *Industrial & Engineering Chemistry Research*, 44(16):6022–6037, August 2005.

J. Forterre and O. Pouliquen. Flow of Dense Granular Media. *Annual Review of Fluid Mechanics*, 40:1–24, 2008.

K. Hong, W. Wang, Q. Zhou, J. Wang, and J. Li. An EMMS-based multi-fluid model (EFM) for heterogeneous gas-solid riser flows: Part I. Formulation of structure-dependent conservation equations. *Chemical Engineering Science*, 75:376–389, June 2012.

Y. Igci and S. Sundaresan. Constitutive Models for Filtered Two-Fluid Models of Fluidized Gas-Particle Flows. *Industrial & Engineering Chemistry Research*, 50(23):13190–13201, 2011.

B. Lu, W. Wang, and J. Li. Searching for a mesh-independent sub-grid model for CFD simulation of gassolid riser flows. *Chemical Engineering Science*, 64(15):3437–3447, August 2009.

J.-F. Parmentier, O. Simonin, and O. Delsart. A functional subgrid drift velocity model for filtered drag prediction in dense fluidized bed. *AIChE Journal*, 58(4):1084–1098, 2012.

S. Schneiderbauer, A. Aigner, and S. Pirker. A comprehensive frictional-kinetic model for gas-particle flows: analysis of fluidized and moving bed regimes. *Chemical Engineering Science*, 80:279–292, 2012a.

S. Schneiderbauer, D. Schellander, A. Löderer, and S. Pirker. Non-steady state boundary conditions for collisional granular flows at flat frictional moving walls. *International Journal of Multiphase Flow*, 43:149–156, July 2012b.

A. Srivastava and S. Sundaresan. Analysis of a frictional-kinetic model for gas-particle flow. *Powder Technology*, 129(1-3):72–85, January 2003.

J. Wang, W. Ge, and J. Li. Eulerian simulation of heterogeneous gassolid flows in CFB risers: EMMS-based sub-grid scale model with a revised cluster description. *Chemical Engineering Science*, 63(6):1553–1571, March 2008.

J. Wang, M. A. van der Hoef, and J. A. M. Kuipers. Coarse grid simulation of bed expansion characteristics of industrial-scale gas-solid bubbling fluidized beds. *Chemical Engineering Science*, 65(6):2125–2131, March 2010.

C. Y. Wen and Y. H. Yu. Mechanics of Fluidization. *Chemical Engineering Progress Symposium Series*, 62:100, 1966.

B. Zou, H. Li, Y. Xia, and X. Ma. Cluster structure in a circulating fluidized bed. *Powder Technology*, 78:173–178, 1994.